Available online at www.sciencedirect.com

ScienceDirect

Journal of Magnesium and Alloys 8 (2020) 510–522

www.elsevier.com/locate/jma

Full Length Article

Microstructural, mechanical and corrosion characterization of an as-cast Mg–3Zn–0.4Ca alloy for biomedical applications

N. Pulido-González[a], B. Torres[a,*], P. Rodrigo[a], N. Hort[b], J. Rams[a]

[a] *Department of Applied Mathematics, Materials Science and Engineering and Electronics Technology, ESCET, Rey Juan Carlos University, C/ Tulipán s/n, 28933 Móstoles, Madrid, Spain*

[b] *Magnesium Innovation Centre, Helmholtz-Zentrum Geesthacht, 21502 Geesthacht, Germany*

Received 19 November 2019; received in revised form 16 January 2020; accepted 7 February 2020
Available online 8 May 2020

Abstract

The as-cast Mg–3Zn–0.4Ca alloy shows a great potential to be used in biomedical applications due to its composition, mechanical properties and biodegradability. Zn and Ca appear naturally in the organism accomplishing vital functions. The alloy consists of an α-Mg matrix and a eutectic composed of α-Mg + $Ca_2Mg_6Zn_3$. The eutectic product enhances the mechanical properties of the studied alloy, causing strengthening and providing superior hardness values. In this alloy, cracks initiate at the intermetallic compounds and progress through the matrix because of the open network formed by the eutectics. Attending to the corrosion results, the eutectic product presents a noble potential compared to the α-Mg phase. For this reason, the corrosion progresses preferentially through the matrix, avoiding the (α-Mg + $Ca_2Mg_6Zn_3$) eutectic product, when the alloy is in direct contact to Hank's solution.

Keywords: Mg–Zn–Ca alloys; Biomaterials; Biodegradable implants; Nanoindentation; Three-point bending test; Corrosion behaviour.

1. Introduction

Magnesium (Mg) has attracted great attention in the biomedical area due to its intrinsic properties, such as density and mechanical properties close to those of the bone and biodegradability. Focusing on the development of Mg biodegradable implants, they must achieve the following requirements: temporary nature, biocompatibility with the surrounding environment, non-toxicity, appropriate mechanical properties to allow total bone repairing and uniform and gradual degradation. It would be also interesting to use a material with an elastic modulus similar to that of natural bone for preventing stress shielding between implant and bone [1–4]. However, the standard electrode potential of Mg (−2.37 V) makes this element react with body fluid, showing an undesirable corrosion rate for the biomedical applications. Alloying constitutes a way to improve the mechanical properties and the corrosion behaviour of Mg and different authors have studied the effect of several alloying elements on magnesium properties [5–8]. The commonly used Mg-based alloys containing Aluminium (Al) are being displaced because of the toxicity and the poor assimilation of Al by the human body [9,10]. Calcium (Ca), zinc (Zn) and manganese (Mn) are considered safe elements for the body as they appear naturally in it. For this reason, Mg-based alloys containing these elements individually or simultaneously are being studied as suitable materials to be used as biomaterials. In this research, a ternary Mg–Zn–Ca alloy has been selected. Zn is essential for the human body and it participates in the correct operation of several systems. Moreover, Zn acts a grain refining agent, mitigates the corrosive effect of nickel (Ni) and iron (Fe) impurities in Mg alloys and can increase the strength by solid solution and precipitation strengthening. Ca is the most abundant mineral in the human body being the main component of the bones. Ca is also associated with

* Corresponding author.
E-mail address: belen.torres@urjc.es (B. Torres).

https://doi.org/10.1016/j.jma.2020.02.007

Table 1
Compositional analysis of the as-cast Mg–3Zn–0.4Ca alloy.

Element	Ca	Zn	Fe	Cu	Ni	Mg
wt.%	0.40	3.14	0.012	0.0015	0.0008	Bal.

the grain refinement of the Mg alloys and the released Ca ions are beneficial for the bone healing process [11,12]. The solubility of Zn and Ca in Mg is 6.2 wt% and 1.3 wt%, respectively. Previous studies have determined the percentages of Ca and Zn that should be added to enhance the mechanical properties and the corrosion rate of magnesium: up to 4 wt% of Zn and less than 1 wt% of Ca [1,13]. It has been proven that an increase in Zn contents leads to a weakening in the corrosion resistance. Also, a higher percentage of Ca produces fragile Mg_2Ca precipitates at grain boundaries [14] and causes problems in the casting process [15], resulting in the worsening of the mechanical properties and corrosion behaviour of the alloy. In order to obtain a good combination of mechanical properties and corrosion behaviour, an as-cast Mg–3Zn–0.4Ca alloy has been selected for this research.

The aim of this work is to reach a deeper knowledge of the as-cast Mg–3Zn–0.4Ca alloy in terms of microstructure, mechanical properties and corrosion behaviour to evaluate its real and promising possibilities in the biomedical field. Mechanical properties were determined by three-point bending and nanoindentation tests. With the first one, crack propagation throughout the sample in real time was observed. The second technique was used to establish the correlation between microstructure and hardness. The corrosion evaluation of the system has also been performed using electrochemical and hydrogen evolution tests. Finally, the detailed corrosion mechanism followed by the as-cast Mg–3Zn–0.4Ca in Hank's solution has been described.

2. Materials and methods

2.1. Materials preparation

Mg–3Zn–0.4Ca alloy was supplied by the Helmholtz Zentrum Geesthacht (Germany) and it was produced by casting [16]. Mg ingots were molten under an argon protective atmosphere with 0.2% vol. SF_6 and held at 720 °C. After that, Ca and Zn were added to the molten Mg. The mix was stirred for 5 min and poured into a mould. The chemical composition of the alloy was analysed by spark emission spectroscopy and atomic absorption spectrometry, as listed in Table 1. Plates of dimensions $30 \times 25 \times 2.5\,mm^3$ were ground with SiC paper (1200 grit), cleaned in an ultrasonic bath for 5 min and dried with hot air.

2.2. Composition and microstructure characterization

The identification of the phases in the as-cast Mg3Zn0.4Ca alloy was performed by an X-ray spectrometer (D8 ADVANCE Bruker) using monochromatic KαCu (1.54056 Å) as the radiation source, operating at a voltage of 40 kV and a current of 40 mA. Diffraction patterns have been recorded in 2θ scan range from 20° to 90°, with a step size of $\Delta(2\theta) = 0.04°$ and 1 s of time per step. The patterns have been indexed with the PDF-4 + 2019 software containing the ICDD (International Centre for Diffraction Data) database.

For the analysis of the microstructural and compositional characteristics of the Mg-based alloy, a Scanning Electron Microscope (SEM, Hitachi S-3400 N) equipped with an Energy Dispersive X-Ray Spectrometer (EDS, Bruker AXS Xflash Detector 5010) was used. Samples were ground with SiC paper, mechanically polished and etched by Nital solution containing 2 wt% of concentrated nitric acid to reveal the microstructure.

TEM analysis was conducted using a JEOL JEM 2100HT microscope operating at 200 kV equipped with a XEDS (OXFORD INCA). Thin foil specimens were prepared for TEM observations using a standard combination of mechanical thinning and ion-beam milling techniques. The PDF-4 + 2019 software containing the ICDD database was used to determine the crystal system, space group and lattice parameters of the samples.

An image analysis program (LAS V4.8) connected to an optical micrograph (OM, Leica DMR) was used to determinate the volume fraction of the secondary phases in the resulting alloy. Six different zones of the as-cast alloy were analysed.

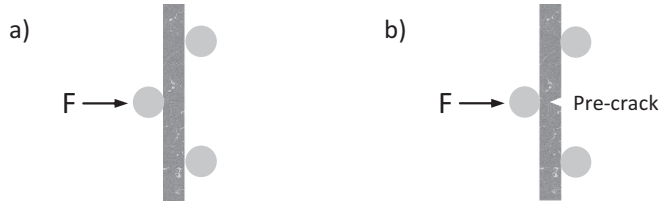

Fig. 1. Three-point bending test configuration: a) without pre-crack and b) with pre-crack.

2.3. Mechanical properties

The load-displacement curves of the samples were obtained using a bending micromachine from Deben installed in a SEM at room temperature. Cracks initiation and progression until fracture were in-situ recorded. The set-up for the test is shown in Fig. 1a.

To calculate the flexural strain and stress, samples with size $2.5 \times 1 \times 30\,mm^3$ were tested. The flexural strain was calculated according to the equation:

$$\varepsilon_f = \frac{6Dd}{L^2} \tag{1}$$

where D is the maximum deflection of the centre of the substrate, d is the height of the sample and L is the support span length. To obtain the flexural stress Eq. (2) was used:

$$\sigma_f = \frac{3L}{2bd^2}F \tag{2}$$

Table 2
Nominal composition of 1 L of Hank's solution (in g).

$CaCl_2$	$MgSO_4$	KCl	KH_2PO_4	NaCl	Na_2HPO_4	D-Glucose
0.1396	0.09767	0.4	0.06	8.0	0.04788	1.0

being F the maximum load and b the width of the tested sample.

The E 399 – 90: *Standard Test Method for Plane-Strain Fracture Toughness of Metallic Materials* [17] was applied to obtain the fracture toughness (K_Q) of notched specimens:

$$K_Q = \left(\frac{P_Q S}{BW^{3/2}}\right) f\left(\frac{a}{W}\right) \quad (3)$$

Where P_Q is the maximum load, S is the span, B and W are the specimen thickness and width respectively, a is the crack length and $f(\frac{a}{W})$ is a defined function. For this test, samples of dimensions $2.5 \times 2 \times 30\,mm^3$ with a pre-crack of 0.3 mm were used according to the orientation shown in Fig. 1b.

A XP Nanoindenter (MTS) was used to perform the nanoindentantion tests using a Berkovich diamond indenter. A matrix of 625 indentations (25×25) with 25 μm of distance between them in x- and y-axis was carried out to obtain the hardness and elastic modulus among the different phases of the as-cast Mg–3Zn–0.4Ca alloy. A maximum load of 2.5 mN was applied for 15 s. Afterwards, the indentations were observed by OM and SEM to identify the characteristics of the microstructure where each indentation was made.

The average value of the elastic modulus of the studied Mg-based alloy was determined by nanoindentation using the continuous stiffness measurement (CSM), which allows the in-depth measurement of the elastic modulus up to 3000 nm by applying a 5 nm harmonic oscillation amplitude and 45 Hz harmonic frequency to the indentation load. Ten indentations in different zones of the sample were performed.

The microhardness of the as-cast Mg–3Zn–0.4Ca alloy was measured using a Microhardness Tester (SHIMADZU HMV-2TE) with applied loads of 980.7 mN ($HV_{0.1}$) for 20 s. Samples were mechanically polished with diamond paste up to 1 μm. The average value was calculated after ten indentations.

2.4. Corrosion evaluation

Electrochemical tests were performed in Hank's Balanced Salt Solution (Hank's solution) at room temperature, using an Autolab PGStat302N potentiostat. The classical three-electrode cell consisted of a silver/silver chloride (Ag/AgCl, KCl 3 M) electrode as the reference electrode, a graphite rod as the counter electrode and the Mg–3Zn–0.4Ca sample with an exposed area of 0.78 cm^2 as the working electrode. The composition of the electrolyte is shown in Table 2.

Before electrochemical testing, samples were ground with 1200 grade SiC emery paper and ultrasonically cleaned in isopropanol for 5 min and dried using hot air.

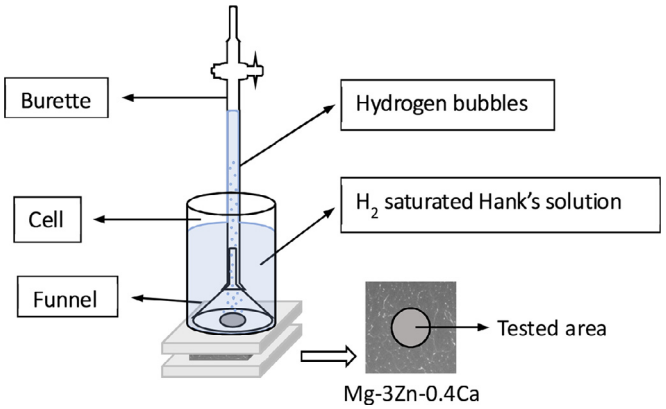

Fig. 2. Schematic assembly for the hydrogen evolution test.

Linear polarization experiments were carried out with a scan rate of 1 mV s^{-1} in the potential range from −10 mV to +10 mV vs. open-circuit potential (*OCP*). The polarization resistance (*Rp*) of the samples was measured at different immersion times: 1, 6, 24, 48, 72, 96 and 168 h. Tests were made by triplicated.

The Tafel extrapolation method was used to determine the corrosion potential (E_{corr}) and the corrosion current density (i_{corr}) of the studied alloy after 1 h of immersion in Hank's solution. For it, a potential range from −400 mV to 800 mV relative to the *OCP* and a scanning rate of 1 mV s^{-1} were used. For the OCP determination, the samples were immersed until a stable value was observed.

Hydrogen evolution tests were carried out on samples of as-cast Mg–3Zn–0.4Ca alloy with dimensions of $30 \times 20 \times 2.5\,mm^3$ that were previously ground with SiC emery paper 1200 grade. The specimens were immersed in 125 mL of Hank's solution saturated with hydrogen in a thermostatic bath at 37 °C. The pH value was kept at 7.4 by bubbling carbon dioxide (CO_2) through the solution. Three different samples were tested to obtain the average value. The corrosion rate P_H in mm y^{-1} was calculated from the hydrogen evolution rate V_H in mL cm^{-2} d^{-1} using Eq. (4) [18]:

$$P_H = 2.279 V_H \quad (4)$$

The set-up for the generated hydrogen collection is shown in Fig. 2. The assembly consists of a funnel that is immersed in a cell containing Hank's solution above the studied sample. The funnel is connected to an inverted burette filled with the same hydrogen saturated Hank's solution. The hydrogen generated during the sample corrosion fills the top part of the burette and displaces the Hank's solution in it. The volume of evolved hydrogen was measured at different times for 336 h. The solution is heated at 37 °C but the external zone of the burette is kept at room temperature.

When the tests were finished, specimens were sprayed with isopropanol to remove the corrosion products that were not adhered on the surfaces and dried using hot air. After that, samples were cross-cut, embedded in conductive resin, mechanically polished (up to 1 μm) and etched in Nital solution

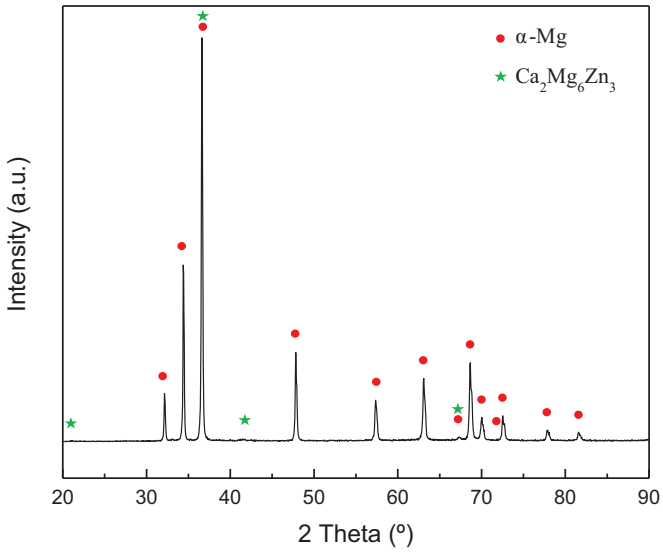

Fig. 3. XRD pattern of the as-cast Mg–3Zn–0.4Ca alloy.

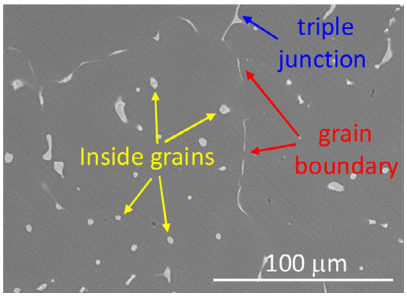

Fig. 4. SEM images showing the eutectic product distribution in the alloy.

to reveal the microstructure. Then, to evaluate the corrosion progression within the microstructure, samples were studied by SEM. The corrosion products were determined by XRD.

3. Results and discussion

3.1. Composition and microstructure characterization

According to the XRD results shown in Fig. 3, the most intense peaks correspond to the α-Mg phase, and the peaks corresponding to the intermetallic compound $Ca_2Mg_6Zn_3$ are also visible. The intensity of these peaks is low compared to that of the matrix due to the small Ca and Zn percentages in the alloy and to the limitation of this technique. As reported in the literature [19], the addition of Zn contents between 3 and 6 wt.% in a Mg–Zn–Ca alloy containing 0.5 wt% of Ca, is proposed to form the α-Mg phase and the (α-Mg + $Ca_2Mg_6Zn_3$) eutectic product [20].

Fig. 4 shows the microstructure of the as-cast Mg–3Zn–0.4Ca alloy. As shown, a secondary phase has been formed and it has precipitated at the grain boundaries with elongated shape, at triple junctions between grains with a thicker shape and with a spherical-like shape within the grains. The measured volume fraction of this phase in the alloy using image analysis was 2.01 ± 0.29 vol%. The α-Mg phase constitutes the rest.

Further research was carried out to analyse the morphology of the secondary phase. Fig. 5a shows the microstructure of the as-cast Mg–3Zn–0.4Ca alloy and a detail of a precipitated particle in which the eutectic morphology can be observed (Fig. 5b). Its shape is similar to the ones observed by other authors in Mg–3 Zn alloys with different Ca additions [21]. The EDS mapping of the selected zone (Fig. 5c) indicates that the matrix is mainly formed by Mg (in red), being Ca and Zn (in green and blue, respectively) mainly placed in the eutectic product. The EDS analysis made on the matrix (Table 3) indicates that it consists of α-Mg with a proportion of Zn and Ca that is determined by the solubility of these elements in Mg. The composition of the precipitates (Table 3) corresponds to that of the intermetallic compound $Ca_2Mg_6Zn_3$.

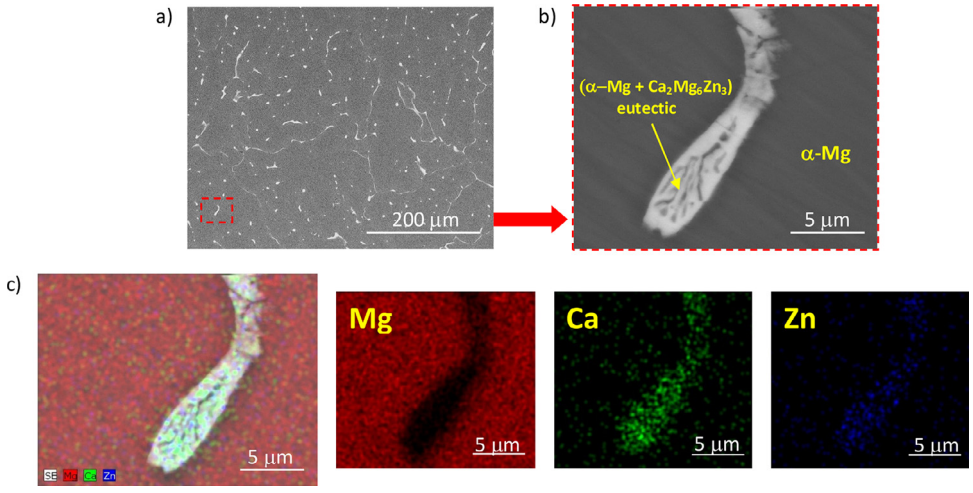

Fig. 5. (a) SEM-SE micrograph of the as-cast Mg–3Zn–0.4Ca alloy; (b) detailed SEM-BSE image of the eutectic product; (c) EDS mapping analysis of the alloy showing the distribution of the Mg, Ca and Zn elements.

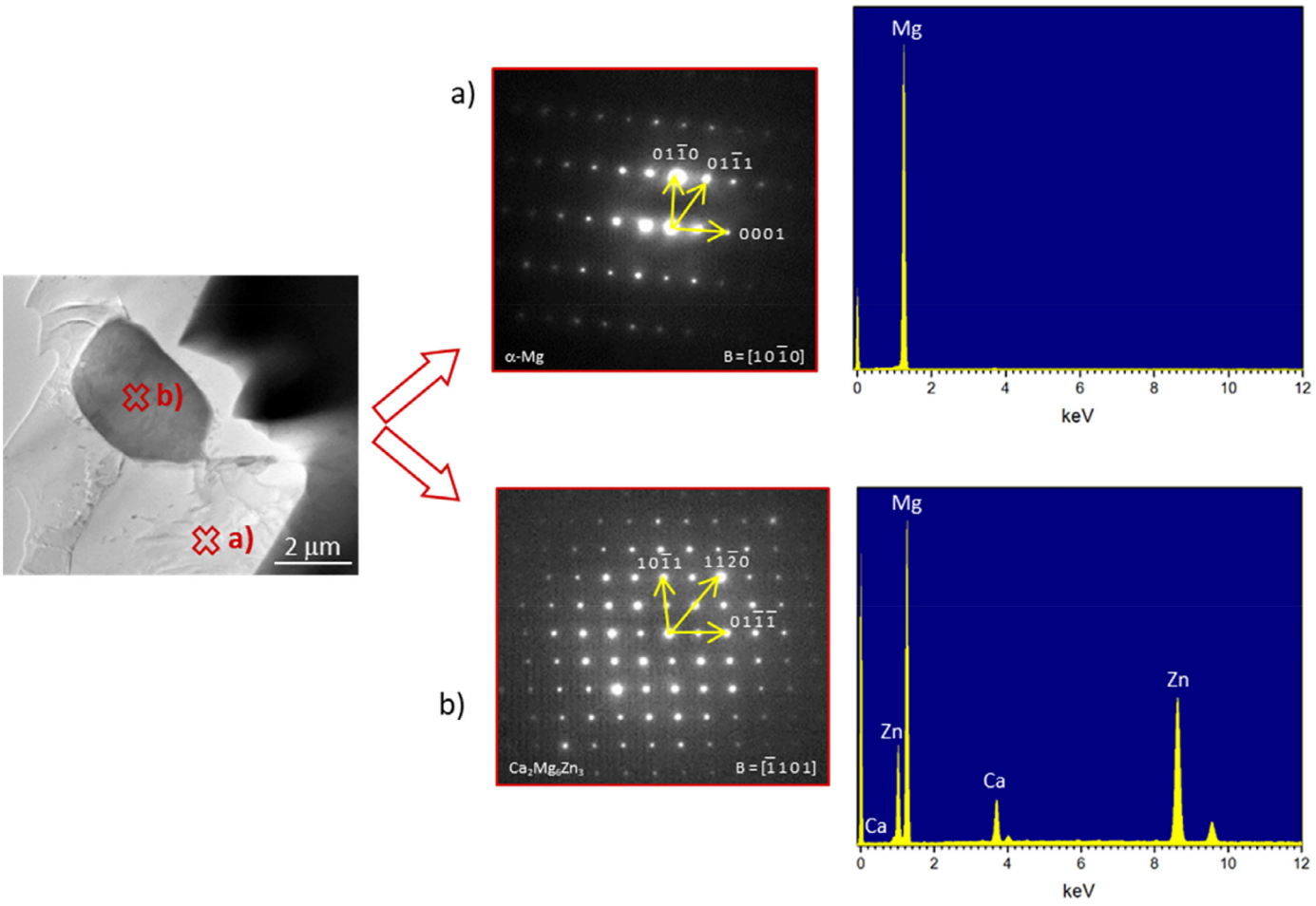

Fig. 6. TEM images, electron diffraction and EDS analysis of the as-cast Mg–3Zn–0.4Ca alloy: a) α-Mg and b) $Ca_2Mg_6Zn_3$.

Table 3
EDS compositional analysis of the matrix and the intermetallic compound.

Phase	Mg (wt%)	Ca (wt%)	Zn (wt%)
α-Mg	91.6 ± 5.5	0.7 ± 0.1	7.7 ± 0.9
$Ca_2Mg_6Zn_3$	45.6 ± 2.4	13.7 ± 0.5	40.7 ± 2.0

Finally, TEM was used to determine the crystalline structure and nature of the as-cast Mg–3Zn–0.4Ca alloy. In Fig. 6, the matrix and one of the particles found in the alloy are analysed, and the electron diffraction patterns are shown. The matrix is basically constituted by Mg, presenting a hexagonal crystalline structure, with the space group P63/mmc and lattice parameters $a = b = 0.322$ nm and $c = 0.523$ nm. The studied precipitated phase corresponds to the $Ca_2Mg_6Zn_3$ intermetallic compound. The crystal system of this ternary compound is also hexagonal, corresponding to the space group $P6_3/mmc$ and the lattice parameters are $a = b = 0.973$ nm and $c = 1.015$ nm. These results were obtained using the ICDD database.

From the combination of the different techniques used (XRD, EDS and TEM), the microstructure of the as-cast Mg-3Zn-0.4Ca alloy has been determined: the matrix is mainly formed by the α-Mg phase in which Ca and Zn are partially dissolved, while the Ca and Zn elements are principally forming the intermetallic compound $Ca_2Mg_6Zn_3$, which appears with an eutectic morphology at grain boundaries with elongated shape and within the grains with a spherical-like shape.

3.2. Three-point bending test

The flexural behaviour of the as-cast Mg–3Zn–0.4Ca alloy was studied using the three-point bending test with a bending micromachine installed inside a SEM. With this assembly, the data collection and the real time crack propagation observation occur simultaneously.

Fig. 7a shows the stress–displacement curves obtained for the samples tested without pre-crack. The maximum value for the flexural stress was 99 ± 7 MPa and the maximum flexural strain was 12.9 ± 0.5%. Samples bended without cracking. These results are similar to those of other Mg-based alloys used in biomedical applications [22]. When the test finished (Fig. 7b), the eutectic products showed some small cracks in the zone subjected to the maximum tensile stress (yellow arrows). It indicates that the intermetallic precipitated phase is much brittle than the matrix. Cracks propagated along the eutectics but stopped at its boundaries, so the lack of

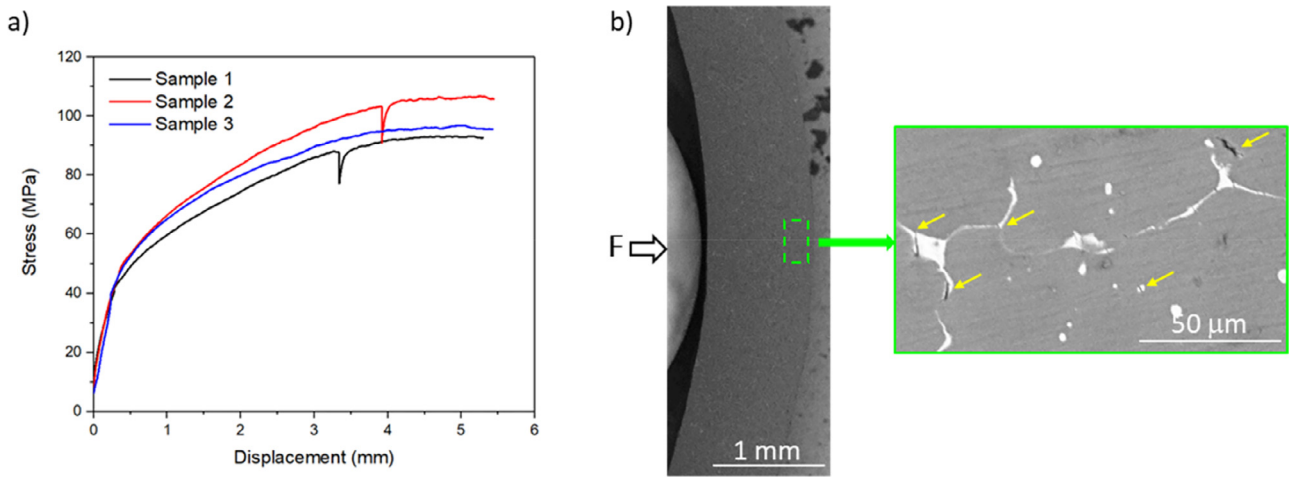

Fig. 7. (a) Stress-displacement curves for the as-cast Mg–3Zn–0.4Ca alloy (the discontinuities in the curve are an artefact caused by stopping the test to obtain in-situ images of the cracks); (b) SEM-SE images of the sample at the final stage of the three-point bending test.

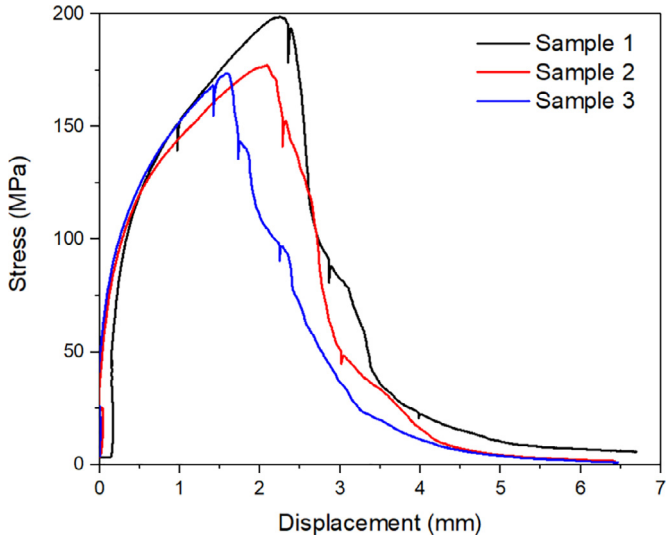

Fig. 8. Stress-displacement curves for the as-cast Mg–3Zn–0.4Ca alloy with pre-crack.

continuity of the eutectics limited the crack propagation through the alloy.

In order to obtain the fracture toughness of the as-cast Mg–3Zn–0.4Ca alloy, an initial pre-crack of 0.3 mm was carried out in the tested samples. The stress–displacement curves obtained after flexural testing with pre-crack are shown in Fig. 8. The average value for the fracture toughness is 5.7 ± 0.3 MPa $m^{1/2}$. This value is similar, but in the lower limit, to those of other Mg-based alloys, whose fracture toughness is usually comprised between 7 and 20 MPa $m^{1/2}$ [23]. In this case, the resulting value is closer to the upper values of the bone (3–6 MPa $m^{1/2}$) [24–26] than other Mg alloys containing aluminium [27–29].

Fig. 9a shows the crack propagating through the as-cast Mg–3Zn–0.4Ca alloy. Cracks initiated at the pre-crack, mainly in precipitates placed at grain boundaries and at triple junctions (yellow arrows), propagating easily where there was a continuous network of eutectic products. However, the limited continuity of the eutectics in this Mg-based alloy stops the crack propagation, so cracks are forced to go through the α-Mg phase, which is less brittle than the eutectic one. Crack-propagation across the matrix takes place by the formation of several microcracks (green arrow) that finally collapse and result in the catastrophic failure of the material. The final stage of the flexural test is shown in Fig. 9b. The precipitated phase presented low plastic deformation, as shown in Fig. 9c. After the breakage, if both parts (R and L) were placed together, only small variations in geometry could be found in the areas corresponding to the matrix, showing that the eutectic products present a complete brittle fracture and that the matrix does not suffer a significant plastic deformation. This is because of the limited energy absorption during the fracture of this alloy.

Fig. 10 represents schematically the previously described mechanism: the intermetallic compounds are crack initiators; cracks firstly propagate along the eutectic (α-Mg + $Ca_2Mg_6Zn_3$) (in black) and then through the matrix (in red), until the tested sample breaks.

3.3. Hardness measurements

The measured average Vickers microhardness of the as-cast Mg–3Zn–0.4Ca alloys at room temperature was 60.7 ± 4.9 $HV_{0.1}$. This result is similar to that observed in other Mg–Zn–Ca alloys [21]. Zn increases the hardness of the Mg alloys via solution hardening and along with Ca produces the precipitation of $Ca_2Mg_6Zn_3$ and grain refinement, which causes precipitation hardening and Hall-Petch strengthening [30–33].

Fig. 11 shows the surface of a sample and its corresponding hardness contour map, as measured by making an indentation matrix of 25×25. Working at the nanoscale, differences in hardness between different phases could be measured. Each of the indentations in the 25×25 matrix was correlated with features of the microstructure and it was found that the dispersion of the eutectics in the alloy has a strong influence

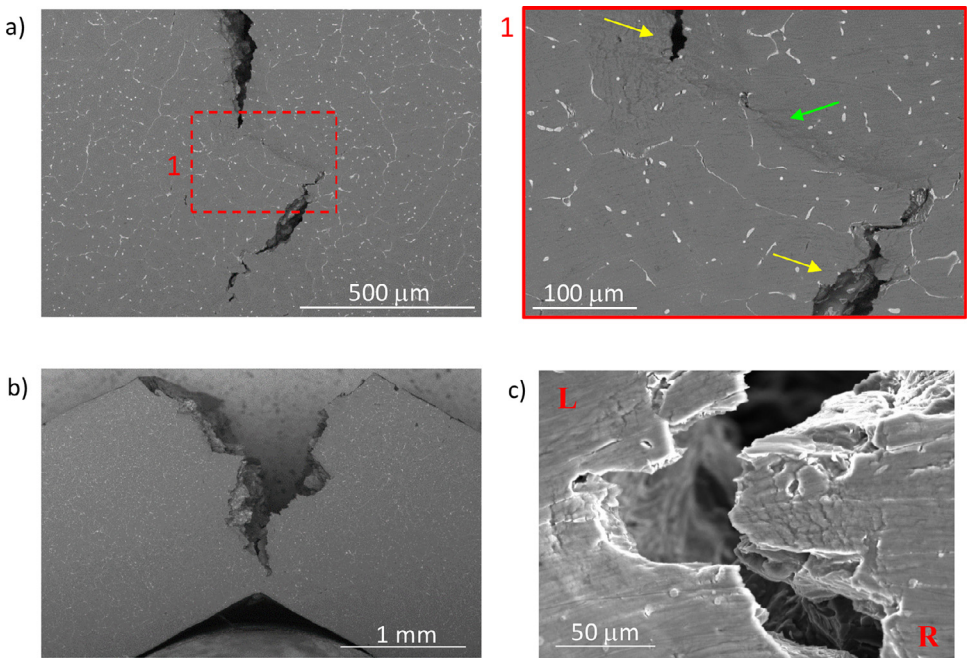

Fig. 9. (a) Crack propagation during three-point bending test; (b) SEM-BSE micrograph of the tested sample; (c) Fracture mechanism of the as-cast Mg–3Zn–0.4Ca alloy.

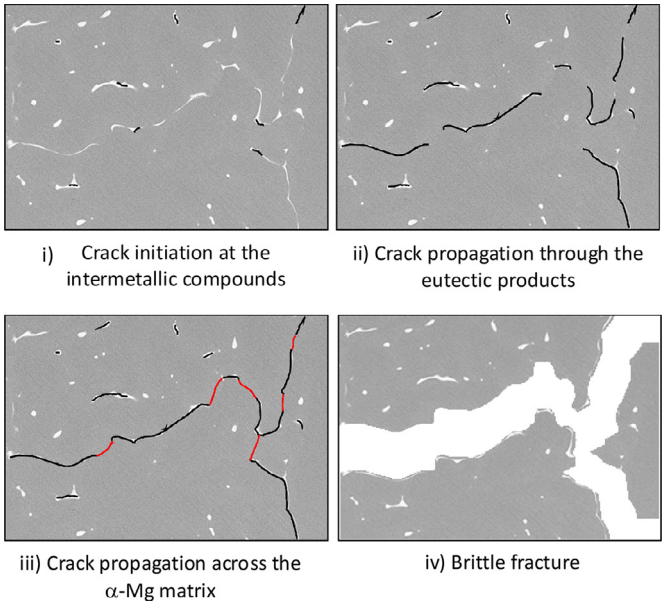

Fig. 10. Schematic illustration of the crack pathway followed by the as-cast Mg–3Zn–0.4Ca alloy showing the different stages that take place during the three-point bending test.

in the resulting hardness. The (α-Mg + $Ca_2Mg_6Zn_3$) eutectic showed the highest hardness values, around 3.5 ± 0.7 GPa. The hardness measured in the areas adjacent to the eutectics was 2.1 ± 0.3 GPa. Finally, the lowest values correspond to the softer phase of the alloy, α-Mg. The relatively high solubility of Zn in Mg increases the measured value of hardness.

Fig. 12a shows five selected indentations of the 25×25 matrix: indentation 1 corresponds to the α-Mg, nanoindentation 2 is placed on the matrix close to a eutectic product, nanoindentations 3 and 4 have the contribution of both, the α-Mg and the eutectic product, and finally, indentation 5 was made at the eutectic. The load-displacement curves of these indentations (Fig. 12b) revealed that the hardness of the (α-Mg + $Ca_2Mg_6Zn_3$) eutectic is higher than that of the matrix. It is also noticeable the effect of the eutectic on the nearby regions, increasing their hardness and resistance.

Fig. 13 shows the relationship between hardness and modulus at maximum load measured for each indentation. Three tendencies are visible, indicating the presence of phases with different behaviour. The values comprised in the yellow ellipse are referred to the eutectic products, the ones in green correspond to the zones surrounding the eutectics and the points in blue are the ones that correspond to the α-Mg phase. As mentioned before, the (α-Mg + $Ca_2Mg_6Zn_3$) eutectic presents the highest hardness and resistance values.

Fig. 14 shows the relation between elastic modulus and displacement into surface of the studied Mg-based alloy using the CSM method. At depths of about 1500 nm, the elastic modulus becomes stable as it is not affected by the indentation size effect, reaching an average elastic modulus of 51.9 ± 2.5 GPa. The resulting value is slightly higher than that of other Mg–Zn–Ca alloys with different Zn and Ca contents and the commonly used AZ31 and AZ91 alloys containing Al [22,34]. The elastic modulus of other metallic alloys used in biomedical applications, as stainless steel, titanium alloys and chromium-cobalt alloys, exceeds the value of 100 GPa [12]. According to the elastic modulus of the bone, ranging from 3

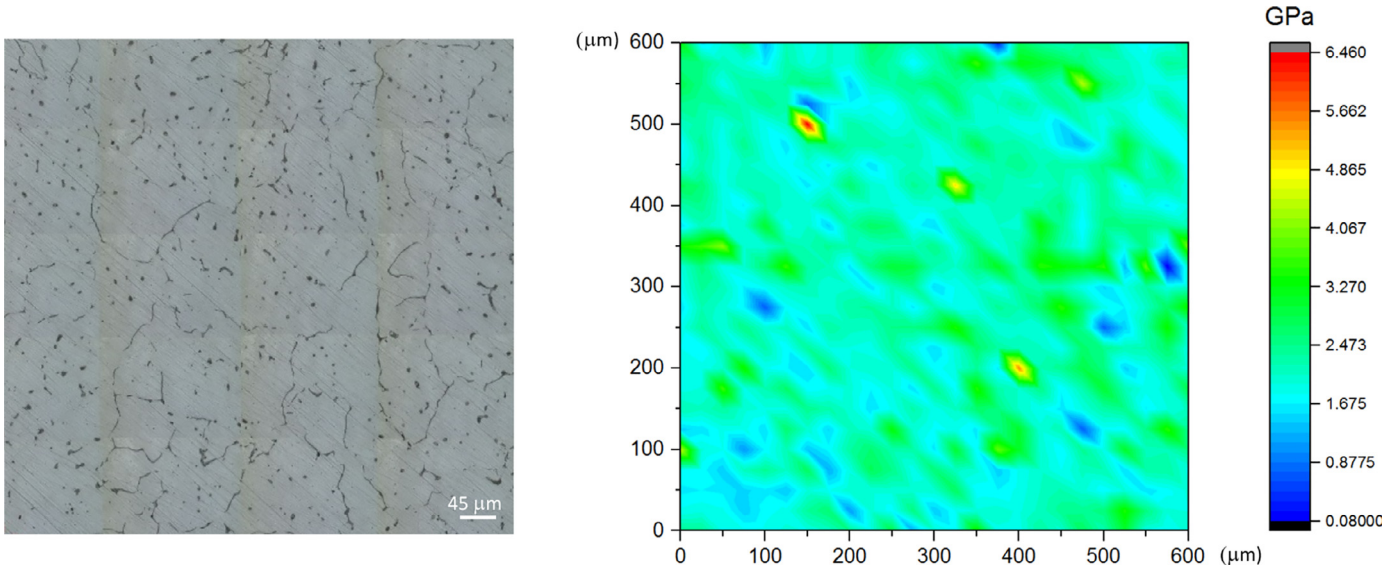

Fig. 11. Hardness contour map corresponding to the 25 × 25 indentation matrix for the as-cast Mg–3Zn–0.4Ca alloy.

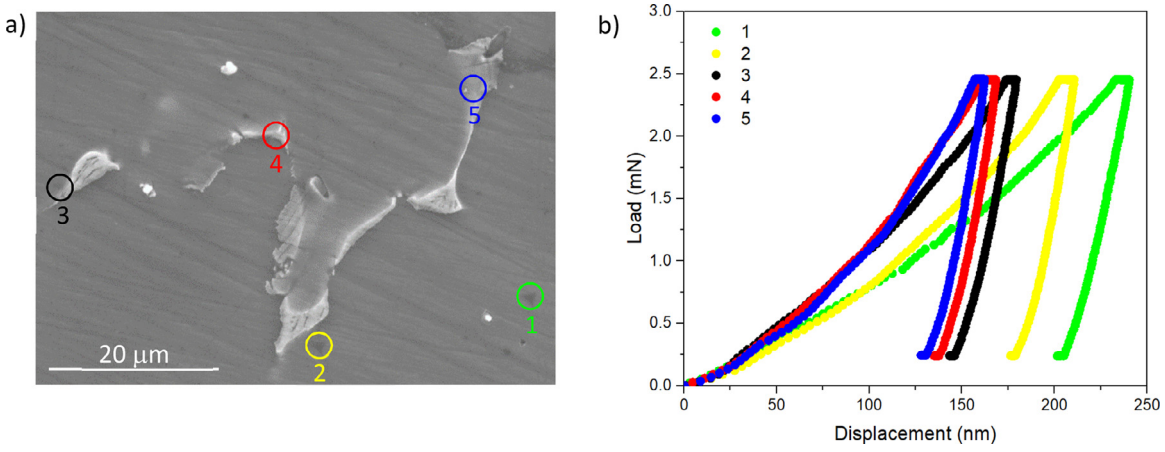

Fig. 12. (a) SEM-SE image of five nanoindentations in the 25 × 25 matrix; (b) Load–displacement curves for the selected indentations.

to 20 GPa [5], Mg–Zn–Ca alloys seem to be more compatible than the previously cited alloys, due to the proximity in the elastic modulus between the alloys containing Zn and Ca and the bone.

3.4. Corrosion behaviour and mechanism

Fig. 15a shows the polarization resistance (*Rp*) of the studied Mg-based alloy after different immersion times in Hank's solution at room temperature. The maximum value of *Rp* was reached at the initial time. After that, corrosion took place and the resistance decreased at 24 h of immersion in the electrolyte. At this time, the formation of a protective layer stabilized the corrosion process at values around 1200 Ωcm^2 .

The anodic-cathodic curves for the as-cast Mg–3Zn–0.4Ca after 1 h of immersion in Hank's solution are shown inFig. 15b. The measured current density was 2.05 µA cm^{-2} and the resulting E_{corr} was −1.53 V. This value is higher than that of other Mg–Ca and Mg–Ca–Zn alloys with a higher amount of Ca and lower Zn content [35,36]. Zn can raise the corrosion potential and improve the corrosion resistance of the alloys. However, further Ca contents generate higher amounts of Mg_2Ca phase, deteriorating the corrosion behaviour of the resulting alloy [19,31,32,37].

Hydrogen evolution is plotted in Fig. 16. The volume of evolved hydrogen increases with immersion time in Hank's solution. From the graph, two different corrosion rates (P_H) can be established: one from 0 to 130 h and the other one, running from 130 to 336 h. Data fitting was performed according to a linear equation:

$$V = V_H \cdot t + b \tag{5}$$

where *V* represents the volume of hydrogen in mL cm^{-2} and *t* is the immersion time in h. Eq. (4) was used to obtain the value of P_H in each interval. For the first section, PH_1 resulted 1.04 mm y^{-1}. This interval is related to the general corrosion mechanism that takes place in the sample. Exceeding 130 h

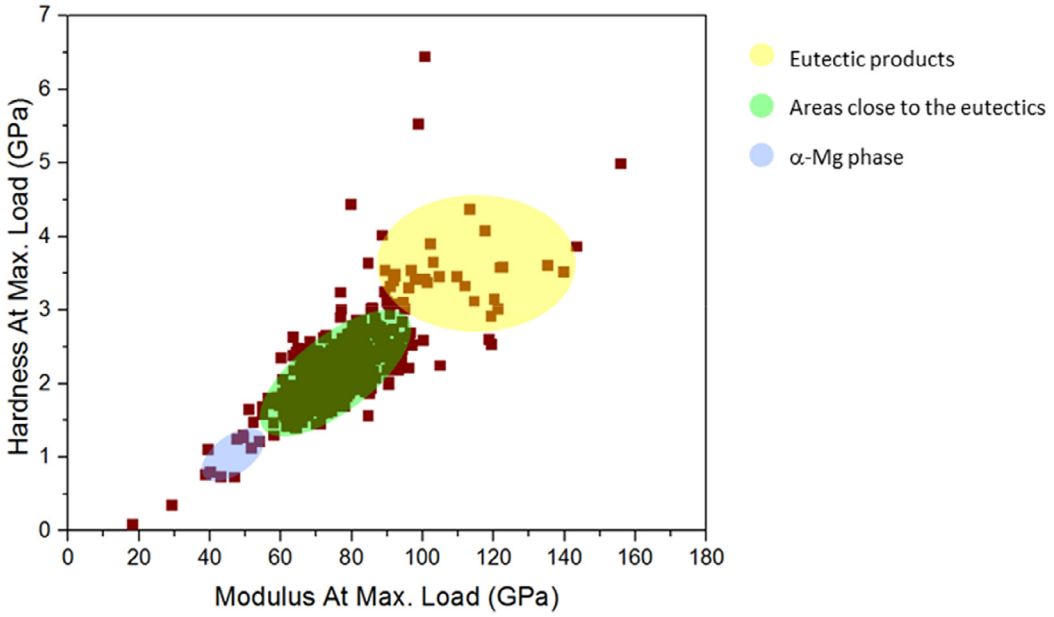

Fig. 13. Relationship between hardness and modulus at maximum load.

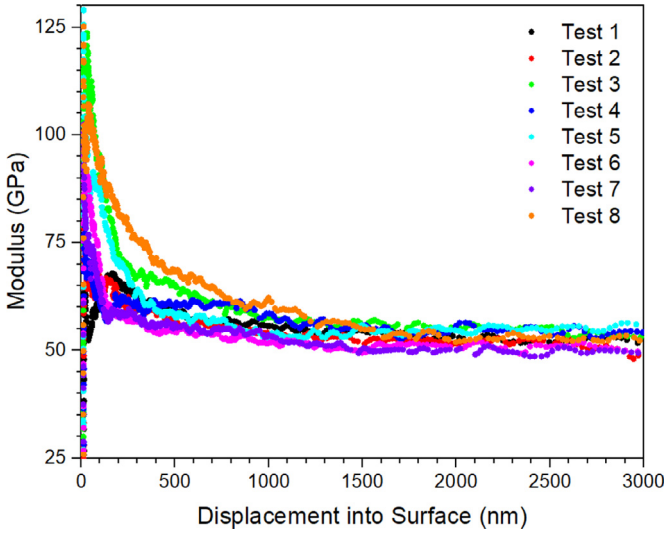

Fig. 14. Modulus in-depth results for the as-cast Mg–3Zn–0.4Ca alloy.

of immersion time, pitting corrosion was the dominant mechanism in the corrosion behaviour of the specimen. For this reason, the contribution of both corrosion mechanisms, uniform and pitting, led to a PH_2 of 3.88 mm y^{-1} after 336 h of immersion in the electrolyte. The volume of hydrogen gas evolved by other Mg-based alloys containing Zn, Ca, Mn, Ce and Al is twice the volume of hydrogen released by the as-cast Mg–3Zn–0.4Ca alloy [38,39]. The hydrogen evolution of the studied Mg-based alloy is also inferior to that of the widely used AZ91 alloy, which presents a P_H of 7.36 mm y^{-1} after 332 h of immersion in Hank's solution [40]. Nevertheless, these values are still high: 0.50 mm y^{-1} was the value established by Erinc et al. [41] for biomaterials used as implants within the body and more strict, the value of 0.02 mm y^{-1} fixed by Song [42] for a material to be tested in the human body.

Corrosion progression was analysed in the cross-section of the sample after 336 h of immersion in Hank's solution, as shown in Fig. 17a,b shows some visible pits with different sizes that progress through the sample. The eutectic products can restrain the corrosion, acting like barriers against corrosion. However, the lack of continuity between the eutectics, which form an open network facilitates the corrosion progress, as observed in Fig. 17c. In this case, the pits have advanced through the sample, crossing it completely from top to bottom. Once the pitting initiates, the corrosion rate increases dramatically, degrading the material. For this reason, controlling the corrosion rate is essential to accomplish with the material requirements for biodegradable implants.

The analysis of the corrosion products formed after immersion in Hank's solution is shown in Fig. 18. The overall reaction taking place during the Mg degradation in contact with an aqueous electrolyte is:

$$Mg + 2H_2O \rightarrow Mg^{2+} + 2OH^- + H_2 \uparrow \quad (6)$$

This reaction indicates that $Mg(OH)_2$ is the main corrosion product and that hydrogen gas is generated, as verified before. According to the EDS mapping analysis, the outer zone was covered by a $Mg(OH)_2$ film, while in the central region, the amount of Ca, O and P was higher than in the rest of the area, suggesting the existence of HA. This fact implies that the as-cast Mg–3Zn–0.4Ca alloy presents good biocompatibility, being essential for a material staying within the body. The XRD technique (Fig. 19) has been used to evaluate the products present on the sample surface. The most intense peaks of the XRD pattern confirmed the presence of $Mg(OH)_2$ in the studied area. The peaks corresponding to HA could not be

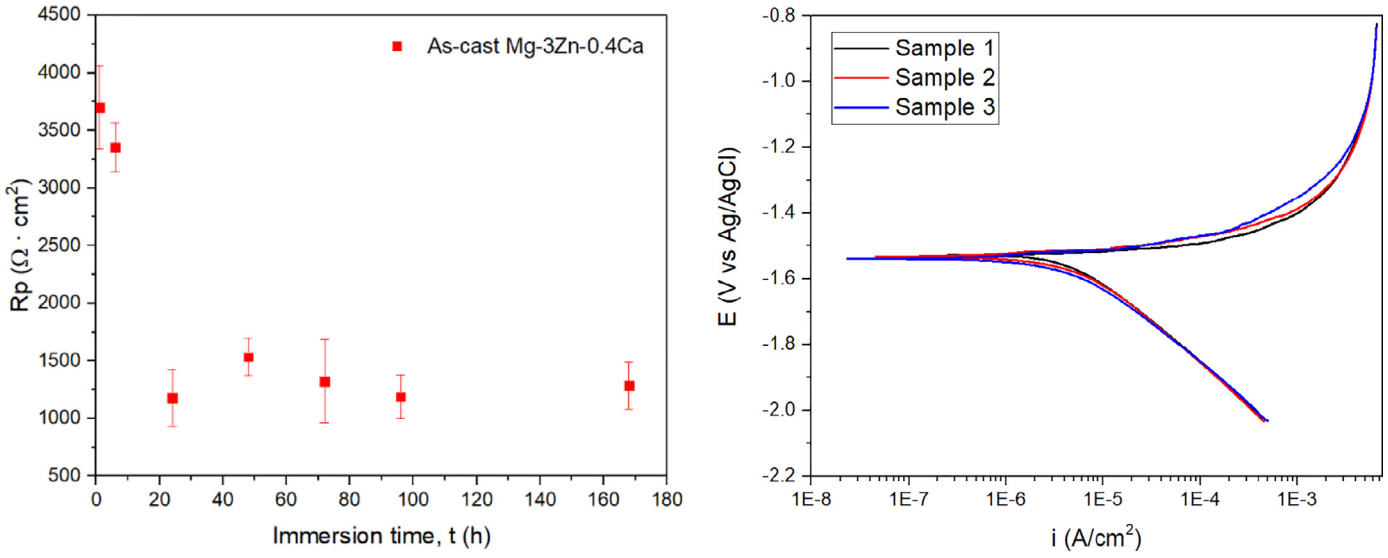

Fig. 15. (a) Polarization resistance and (b) Potentiodynamic polarization curves of the as-cast Mg–3Zn–0.4Ca alloy in Hank's solution at room temperature.

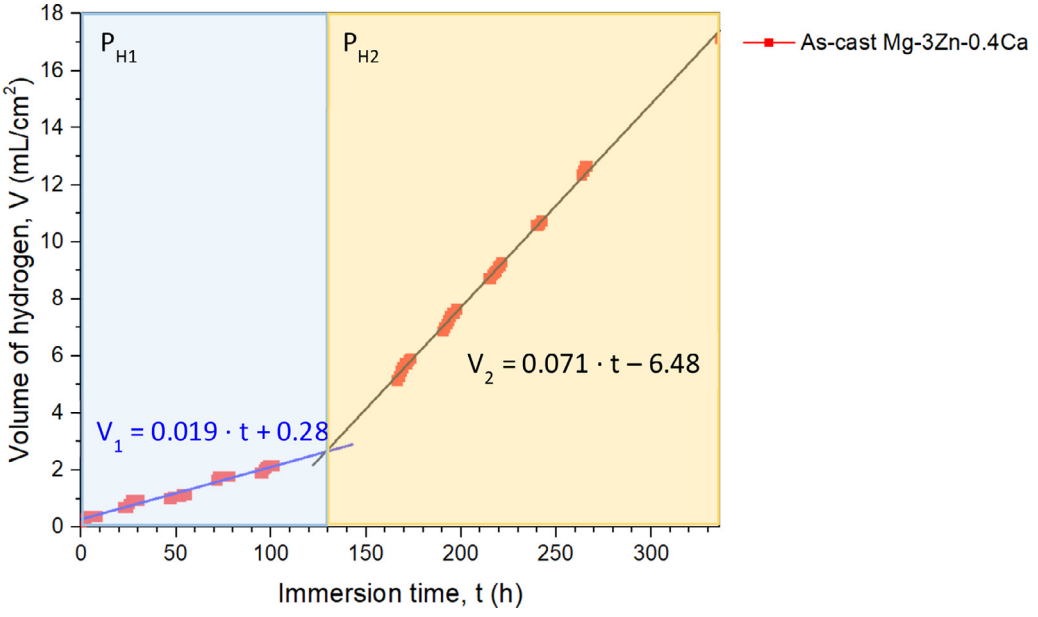

Fig. 16. Determination of the volume of evolved hydrogen after 336 h of immersion in Hank's solution at 37 °C.

distinguished because the amount of HA formed was much lower than that of the $Mg(OH)_2$.

The corrosion process suffered by the as-cast Mg–3Zn–0.4Ca after 336 h of immersion in Hank's solution at 37 °C is represented in Fig. 20. The corrosion potential of the α-Mg matrix is more negative than that of the eutectic (α-Mg + $Ca_2Mg_6Zn_3$) [20,35,43], so the (Mg + $Ca_2Mg_6Zn_3$) eutectic acts as a cathode while the α-Mg matrix is the anode in the alloy. For this reason, the matrix corrodes, acting the eutectics as temporal barriers against corrosion. Fig. 20a shows the first stage of the corrosion mechanism. At this point, the corrosion is uniform and a protective layer of $Mg(OH)_2$ is formed on the exposed surface, which stabilizes the corrosion rate of the alloy [44]. The breakage of this layer due to the generation of hydrogen bubbles allows the chloride ions to penetrate through it, reaching the substrate, as shown in Fig. 20b. At this time, the corrosion advances preferentially following a pitting corrosion mechanism, much more severe than the general corrosion mechanism [12,45]. It is known that chloride ions accelerate the corrosion rate of the Mg-based alloys [46]. The corrosion progress is also strongly dependant on the amount and distribution of the eutectics in the alloy. The open network formed by the eutectic products in the as-cast Mg-3Zn-0.4Ca alloy accelerates the corrosion progression that advances quickly through the matrix, acting the (α-Mg + $Ca_2Mg_6Zn_3$) eutectics as local corrosion

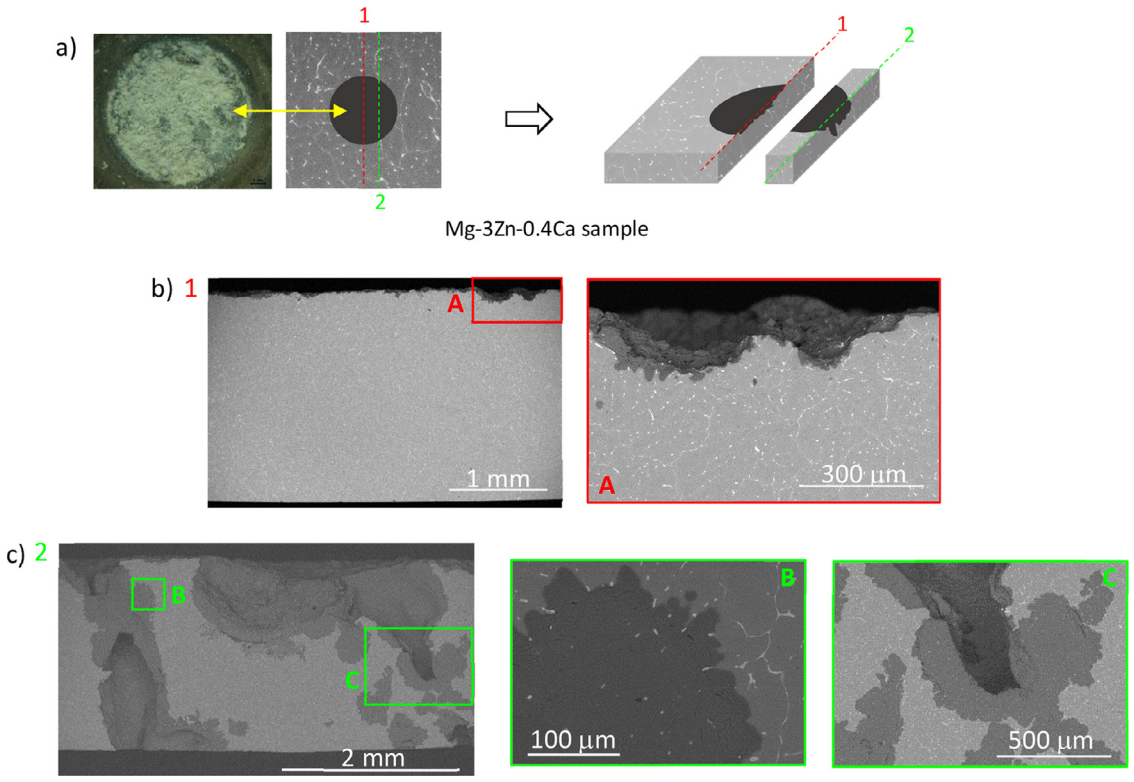

Fig. 17. (a) Image of the surface and illustration of two different cross-sections of the sample after 336 h of immersion in Hank's solution; (b) SEM images of the corroded area in the cross-Section 1; (c) SEM micrographs of the corroded region in the cross-Section 2.

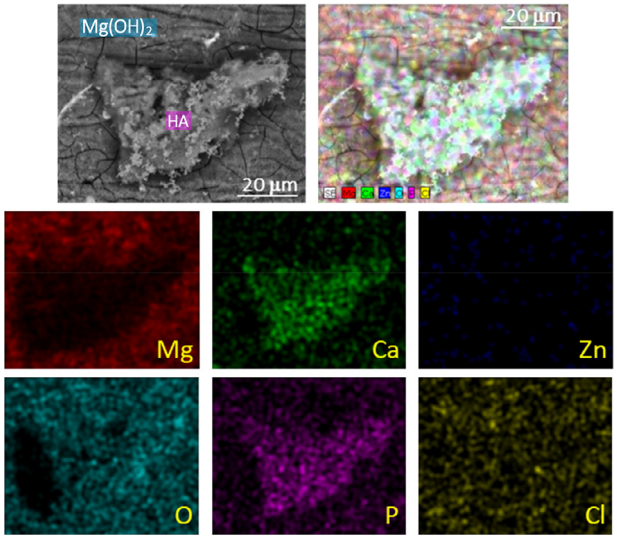

Fig. 18. EDS mapping analysis of a localized zone of the as-cast Mg–3Zn–0.4Ca alloy after immersion in Hank's solution.

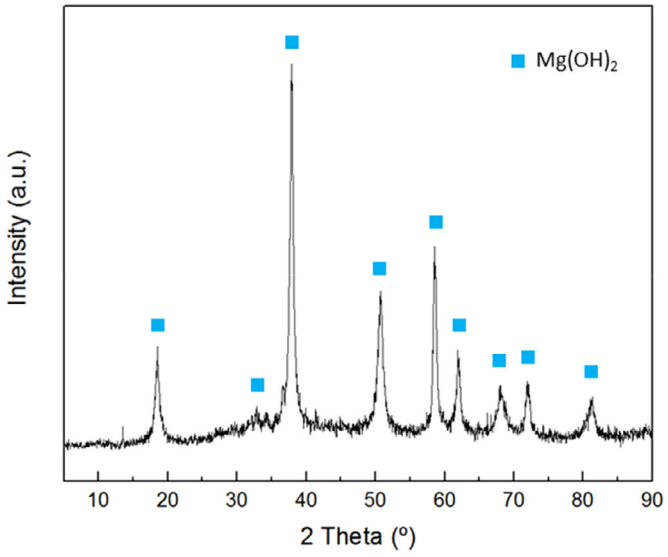

Fig. 19. XRD pattern of the corrosion products formed over the sample after 336 h of immersion in Hank's solution at 37 °C.

barriers, restraining the corrosion [35]. This behaviour has also been detected for the $Mg_{17}Al_{12}$ (β phase) formed in the AZ91 alloy [20]. Finally, Fig. 20c represents the formation of HA in the area in contact to the electrolyte, due to the precipitation of phosphates as a result of a pH rise in the environment.

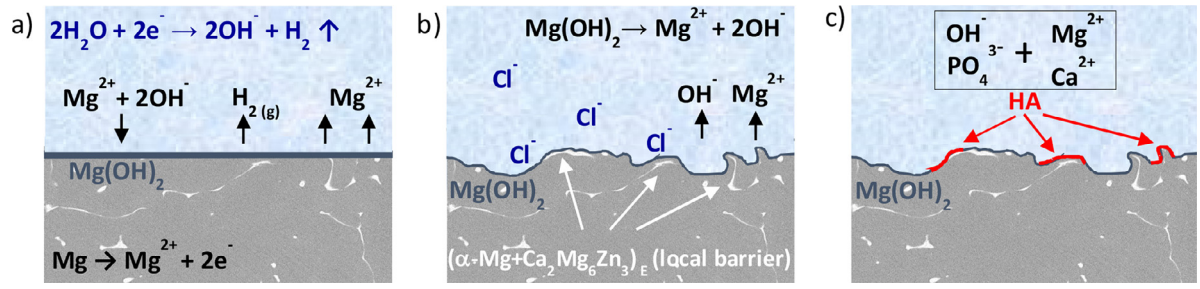

Fig. 20. Schematic illustration of the corrosion process evolution of the as-cast Mg–3Zn–0.4Ca in contact to Hank's solution: (a) galvanic reaction between substrate and H_2O and generation of OH^- and H_2 gas; (b) dissolution of the $Mg(OH)_2$ protective layer and (α-Mg + $Ca_2Mg_6Zn_3$) eutectics acting as local barriers against corrosion; (c) precipitation of hydroxyapatite.

4. Conclusions

The main conclusions obtained in this research are indexed:

(1) The as-cast Mg–3Zn–0.4Ca alloy is mainly formed by the α-Mg matrix and a small volume fraction of eutectic (α-Mg + $Ca_2Mg_6Zn_3$) products.
(2) The studied alloy shows a brittle fracture mechanism. Cracks initiate at the eutectics, which are more brittle than the matrix and propagate through them. The lack of continuity of the eutectic products forces the cracks to progress across the α-Mg phase, slowing the crack progression.
(3) The hardness and elastic modulus of the eutectics are higher than the matrix ones. These eutectic products influence the adjacent zones, where the hardness and elastic modulus values are intermediate between the eutectic and the α-Mg.
(4) The corrosion evolution of the as-cast Mg–3Zn–0.4Ca alloy can be divided into two different intervals according to the hydrogen evolution test. The first section, which lasts 130 h, is related to the initial phase of corrosion suffered by the Mg-based alloy when it is immersed in Hank's solution. Exceeding this time, the formation of small pits on the exposed surface increases the corrosion rate.
(5) The study of the corrosion products after 336 h of immersion in Hank's solution shows that they are mainly constituted of $Mg(OH)_2$ with small amounts of HA.
(6) The eutectic formed acts as a barrier to the corrosion progress but its effect is limited because it forms an open network. On the other hand, the discontinuities in the eutectic increases the toughness on the material. This shows that the improvement of the material can be reached by the control of its microstructure, a compromise between corrosion and fracture behaviour might be assumed.

Acknowledgments

The authors would like to acknowledge the financial support from the Agencia Estatal de Investigación (Project RTI2018-096391-B-C31), Comunidad de Madrid (Project ADITIMAT-CM S2018/NMT-4411) and the FPU grant (15/03606) from the Ministerio de Educación, Cultura y Deporte, Spain.

References

[1] S. Zhang, et al., Mater. Sci. Eng. C 29 (6) (2009) 1907–1912 https://doi.org/10.1016/j.msec.2009.03.001.
[2] E. Willbold, et al., J. Biomed. Mater. Res. - Part A 105 (1) (2017) 329–347 https://doi.org/10.1002/jbm.a.35893.
[3] A. Atrens, et al., J. Magnes. Alloy. 1 (3) (2013) 177–200 https://doi.org/10.1016/j.jma.2013.09.003.
[4] R. Radha, et al., J. Magnes. Alloy. 5 (3) (2017) 286–312 https://doi.org/10.1016/j.jma.2017.08.003.
[5] M.P. Staiger, et al., Biomaterials 27 (9) (2006) 1728–1734 https://doi.org/10.1016/j.biomaterials.2005.10.003.
[6] N. Sezer, et al., J. Magnes. Alloy. 6 (1) (2018) 23–43 https://doi.org/10.1016/j.jma.2018.02.003.
[7] K. Gusieva, et al., Int. Mater. Rev. 60 (3) (2015) 169–194 https://doi.org/10.1179/1743280414Y.0000000046.
[8] T. Li, et al., J. Magnes. Alloy. 2 (2) (2014) 181–189 https://doi.org/10.1016/j.jma.2014.05.006.
[9] S. Maya, et al., Biomed. Pharmacother. 83 (2016) 746–754 https://doi.org/10.1016/j.biopha.2016.07.035.
[10] P. Nayak, Environ. Res. 89 (2) (2002) 101–115 https://doi.org/10.1006/enrs.2002.4352.
[11] H.R. Bakhsheshi-Rad, et al., Mater. Corros. 65 (12) (2014) 1178–1187 https://doi.org/10.1002/maco.201307588.
[12] S. Agarwal, et al., Mater. Sci. Eng. C 68 (2016) 948–963 https://doi.org/10.1016/j.msec.2016.06.020.
[13] S. Zhang, et al., Acta Biomater. 6 (2) (2010) 626–640 https://doi.org/10.1016/j.actbio.2009.06.028.
[14] N. Li, et al., J. Mater. Sci. Technol. 29 (6) (2013) 489–502 https://doi.org/10.1016/j.jmst.2013.02.005.
[15] F. Witte, et al., Curr. Opin. Solid State Mater. Sci. 12 (5–6) (2008) 63–72 https://doi.org/10.1016/j.cossms.2009.04.001.
[16] F.R. Elsayed, et al., Mater. Sci. Forum 690 (2011) 65–68 https://doi.org/10.4028/www.scientific.net/MSF.690.65.
[17] W. Conshohocken, "ASTM Standard E 399-90. Standard Test Method for Plane-Strain Fracture Toughness of Metallic Materials, United States: ASTM INternational, 1997.
[18] Z. Shi, et al., Corros. Sci. 53 (1) (2011) 226–246 https://doi.org/10.1016/j.corsci.2010.09.016.
[19] H.R. Bakhsheshi-Rad, et al., Corros. Sci. 64 (2012) 184–197 https://doi.org/10.1016/j.corsci.2012.07.015.
[20] Y. Lu, et al., Mater. Sci. Eng. C 48 (2015) 480–486 https://doi.org/10.1016/j.msec.2014.12.049.
[21] K. Kubok, et al., Arch. Metall. Mater. 58 (2) (2013) 329–333 https://doi.org/10.2478/v10172-012-0193-2.

[22] J. Chen, et al., J. Mech. Behav. Biomed. Mater. 87 (2018) 68–79 https://doi.org/10.1016/j.jmbbm.2018.07.022.
[23] V. Kaushik, et al., Mater. Sci. Eng. A 590 (2014) 174–185 https://doi.org/10.1016/j.msea.2013.10.018.
[24] R.K. Nalla, et al., J. Biomech. 38 (7) (2005) 1517–1525 https://doi.org/10.1016/j.jbiomech.2004.07.010.
[25] P. Zioupos, et al., Bone 22 (1) (1998) 57–66 https://doi.org/10.1016/S8756-3282(97)00228-7.
[26] J.B. Phelps, et al., J. Biomed. Mater. Res. 51 (4) (2000) 735–741 https://10.1002/1097-4636(20000915)51:4⟨735::aid-jbm23⟩3.0.co;2-g.
[27] C. Taltavull, et al., J. Mater. 55 (2014) 361–365 https://doi.org/10.1016/j.matdes.2013.10.010.
[28] B. Kim, et al., Mater. Sci. Eng. A 527 (24–25) (2010) 6745–6757 https://doi.org/10.1016/j.msea.2010.07.016.
[29] X. Yu, et al., Eng. Fail. Anal. 58 (Part 2) (2015) 322–335 https://doi.org/10.1016/j.engfailanal.2015.04.020.
[30] S. Kim, et al., J. Alloys Compd. 766 (2018) 994–1002 https://doi.org/10.1016/j.jallcom.2018.06.088.
[31] Y. Sun, et al., Mater. Des. 34 (2012) 58–64 https://doi.org/10.1016/j.matdes.2011.07.058.
[32] H. Reza, et al., Appl. Mech. Mater. 121-126 (2012) 568–572 https://10.4028/www.scientific.net/AMM.121-126.568.
[33] A. Bahmani, et al., J. Magnes. Alloy. 7 (1) (2019) 38–46 https://doi.org/10.1016/j.jma.2018.11.004.
[34] B. Homayun, et al., J. Alloys Compd. 607 (2014) 1–10 https://doi.org/10.1016/j.jallcom.2014.04.059.
[35] D. Zander, et al., Corros. Sci. 93 (2015) 222–233 https://doi.org/10.1016/j.corsci.2015.01.027.
[36] Z. Xu, et al., Mater. Sci. Eng. B Solid-State Mater. Adv. Technol. 176 (20) (2011) 1660–1665 https://doi.org/10.1016/j.mseb.2011.06.008.
[37] L. Wang, et al., Trans. Nonferrous Met. Soc. China" 26 (3) (2016) 704–711 https://doi.org/10.1016/S1003-6326(16)64182-1.
[38] F. Zhang, et al., J. Rare Earth 33 (1) (2015) 93–101 https://doi.org/10.1016/S1002-0721(14)60388-4.
[39] Z. Chun-Yan, et al., Surf. Coatings Technol. 204 (21–22) (2010) 3636–3640 https://doi.org/10.1016/j.surfcoat.2010.04.038.
[40] N.I. Zainal Abidin, et al., Corros. Sci. 53 (11) (2011) 3542–3556 https://doi.org/10.1016/j.corsci.2011.06.030.
[41] M. Erinc, et al., Magnes. Technol. (2009) 209–214.
[42] G. Song, Corros. Sci. 49 (4) (2007) 1696–1701 https://doi.org/10.1016/j.corsci.2007.01.001.
[43] W. Du, et al., J. Magnes. Alloy. 6 (1) (2018) 1–14 https://doi.org/10.1016/j.jma.2018.01.004.
[44] A. Mohamed, et al., J. Magnes. Alloy. 7 (2) (2019) 249–257 https://doi.org/10.1016/j.jma.2019.02.007.
[45] G.L. Song, et al., Adv. Eng. Mater. 1 (1) (1999) 11–33 https://doi.org/10.1002/(SICI)1527-2648(199909)1:1⟨11::AID-ADEM11⟩3.0.CO;2-N.
[46] Q. Li, et al., Mater. Sci. Eng. C 57 (2015) 349–354 https://doi.org/10.1016/j.msec.2015.08.008.